UC Berkeley
UC Berkeley Previously Published Works

Title

Depth migration of seasonally induced seismicity at The Geysers geothermal field

Permalink

https://escholarship.org/uc/item/6x29k3d6

Journal

Geophysical Research Letters, 43(12)

ISSN

0094-8276

Authors

Johnson, Christopher W
Totten, Eoghan J
Bürgmann, Roland

Publication Date

2016-06-28

DOI

10.1002/2016gl069546

Peer reviewed

Depth migration of seasonally induced seismicity at The Geysers geothermal field

Christopher W. Johnson[1], Eoghan J. Totten[2], and Roland Bürgmann[1]

[1] Berkeley Seismological Laboratory and Department of Earth and Planetary Science, University of California, Berkeley, California, USA, [2] Department of Earth Science and Engineering, Imperial College London, London, UK

Correspondence to: C. W. Johnson, cwj@seismo.berkeley.edu

Abstract

Seismicity from injected fluids provides insight into the hydraulically conductive fracture network at The Geysers (TG), California, geothermal reservoir. Induced earthquakes at TG result from both thermoelastic and poroelastic stresses as injected fluids cool the rocks and increase pore pressure. The spatiotemporal evolution of $M \geq 1.5$ seismicity is characterized as a function of depth in the northwest and southeast regions of TG to develop time-dependent earthquake rates using an epidemic-type aftershock sequence model. The seismicity and injection follow an annual cycle that peaks in the winter months and is correlated by depth. The results indicate a time lag of ≤ 6 months for fluids to migrate >3 km below the injection depth. Water injection is the main cause of seismicity as fluids penetrate into the reservoir. Our results suggest that a steeply dipping fracture network of hydraulically conductive faults allows fluid migration to a few kilometers below the point of injection.

1 Introduction

The Geysers (TG) geothermal reservoir, located in Northern California (Figure 1), began operations in 1960 and is the largest geothermal power facility in the world. A decrease in reservoir steam pressure beginning in 1987 led to the construction of tertiary wastewater supply pipelines in 1998 and 2004 to augment existing water injection facilities. Large-volume fluid injection into the subsurface has long been recognized to induce earthquake activity in the host rock [*Evans*, 1966; *Healy et al.*, 1968]. TG is no exception with fluid injection known to induce seismicity [*Eberhart-Phillips and Oppenheimer*, 1984; *Majer et al.*, 2007; *Marks et al.*, 1978; *Stark*, 1991; *Trugman et al.*, 2016]. The focus of this study is to quantify the seismicity rates at the TG using time series characterizing specific depth intervals within the reservoir to illuminate the first-order depth migration of fluids in response to injection.
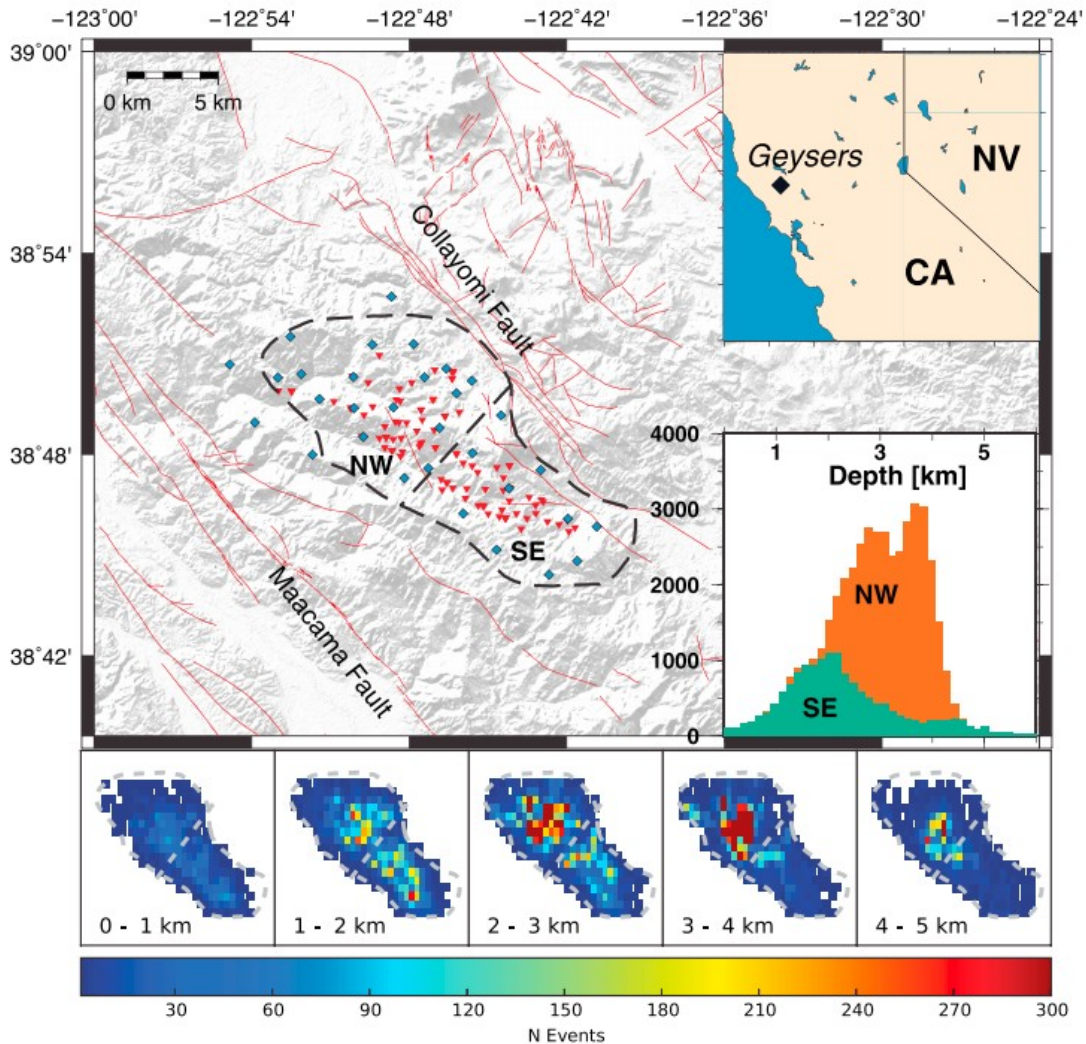
Figure 1. The Geysers (TG) geothermal field in Northern California (top-right insert) lies between the Maacama Fault and Collayomi Fault. The reservoir is outlined with a black dashed line and divided into NW and SE regions by the dashed line across the reservoir. Blue diamonds indicate the local seismic network, and red inverted triangles are the active injection wells during 2005–2015. Red lines are the USGS mapped faults (http://earthquake.usgs.gov/hazards/qfaults/). The bottom right insert is the depth distribution for the $M \geq 1.5$ earthquakes in the NW shown in orange and SE shown in green between 2005 and 2015. The five bottom plots show the total number of $M \geq 1.5$ catalog events by color per 0.75 km grid cell for the corresponding depth interval.

TG is a subhydrostatic vapor reservoir of fractured Franciscan metagraywacke above a Pleistocene felsite intrusion [*Hartline et al.*, 2015]. The normal reservoir extends to a depth of ~2.5 km with a temperature of ~240 °C in both the northwest (NW) and southeast (SE) regions of TG. In the NW a high-temperature zone (HTZ) exists from ~2.5 to 4.0 km depth, where temperatures increase to ~340 °C [*Beall et al.*, 2010; *Stark*, 2003; *Walters and Combs*, 1992]. The injection interval depths at TG for the largest injection wells are within the upper 2.1 km of the reservoir [*Gritto et al.*, 2014]. Induced seismicity near the injection and production wells is more common in the NW than the SE [*Beall et al.*, 2010]. *Beall and Wright* [2010] identify a boundary that divides TG into NW and SE regions based on the extent of the HTZ and the location of 90% of the $M \geq 3$ seismicity. The induced seismicity in the NW extends to ~5 km depth with a time lag of 3–5

months following peak injection, suggesting that fluids penetrate into the HTZ [*Beall et al.*, 2010; *Stark*, 2003].

In this study, we characterize seismicity at TG by depth and quantify the time lag as fluids migrate deeper into the reservoir. Seismicity rates can be used to detect and characterize transient stresses [*Hainzl and Ogata*, 2005; *Marsan et al.*, 2013], in particular forcing from fluid injection and extraction [*Brodsky and Lajoie*, 2013]. We explore the fluid migration from the injection interval depth to greater depths by correlating the seismicity rate time series with the gross injection and production monthly totals. Our objective is to characterize the large-scale spatiotemporal patterns of the induced seismicity in the SE and NW and to compare our results to site-specific geomechanical models at TG that describe thermoelastic and poroelastic strains related to injection [*Jeanne et al.*, 2014; *Kwiatek et al.*, 2015]. We present results that support the migration of fluids deeper into the reservoir following an annual cycle of large-volume injection.

2 Data

2.1 Seismicity Catalog

In 2003 the Lawrence Berkeley National Laboratory (LBNL) began operating a 31-station monitoring array at TG for microseismicity detection. The seismicity catalog produced by LBNL is available from the Northern California Earthquake Data Center using the Enhanced Geothermal Systems Earthquake Catalog search (http://ncedc.org/egs/catalog-search.html, last accessed on 01 December 2015). The catalog is limited to the active production field (Figure 1) and contains 360,307 $M_L \geq 0$ events from 01 January 2005 to 31 December 2014, with 13 $M_L \geq 4.0$ events in the study area. Event hypocentral locations are obtained using standard single-event location techniques with SimulPS [*Thurber*, 1983] for a three-dimensional velocity structure that is updated annually [*Hutchings et al.*, 2015]. Using the reported errors, we estimate the mean horizontal and vertical uncertainties of 210 m and 400 m, respectively, for the events used in this study. We estimate a catalog magnitude of completeness of M_c1.1 using the maximum curvature method [*Wiemer and Wyss*, 2000] and a b value of 1.325 ± 0.007 using the maximum likelihood method [*Aki*, 1965; *Bender*, 1983] with 2σ confidence intervals [*Shi and Bolt*, 1982] (see Figure S1 in the supporting information). To ensure a complete catalog and stability for the seismicity modeling presented in section 3, we implement a magnitude cutoff of M_L1.5 and use the remaining 60,703 earthquakes during the 10 year study period.

For the analysis we separate TG into NW and SE regions [*Beall and Wright*, 2010; *Convertito et al.*, 2012] as outlined in Figure 1, and 94% of the earthquakes are located at a shallow depth of 0–5 km. When the events are separated by region, the depth distributions indicate shallower events in the SE with the majority occurring at a depth interval of 1–2 km (see inset histogram in Figure 1). The NW region contains 66% of the events, and there is a bimodal distribution of depths with peaks at ~2.5 km and ~4.0 km depth,

which agrees with long-term trends for the depth distribution at higher magnitudes in the reservoir [*Trugman et al.*, 2016]. Additionally, in Figure 1 we show the spatial distribution of earthquakes at 1 km depth intervals for a 0.75 km square grid. The spatial distribution by depth in Figure 1 shows that the concentration of earthquakes correlates with the locations of injection wells and that the seismicity deepens from SE to NW.

2.2 The Geysers Injection Well Records

The California Department of Conservation Division of Oil, Gas, and Geothermal Resources is the state repository for all nonconfidential geothermal field records (http://www.conservation.ca.gov/dog/geothermal/). The data are publically available and records for TG are available from 1997 to 2014. We obtained monthly injection and production data between January 2005 to December 2014 and make no assumptions about unreported wells. We assemble the data as a time series for each well, and the gross total mass is summed for the NW and SE regions of TG (Figure 1). The records do not include the injection well depth, and we rely on reported injection interval depths <2.1 km for 49 highest-volume injection wells throughout the reservoir [*Gritto et al.*, 2014]. From this we infer that in the NW >95% of the injection depths shown are in the injection interval between 0.9 and 1.5 km, and in the SE >90% of the injections occur between 0.0 and 0.9 km. The subsurface locations of the wells do not deviate by more than 1 km from the surface wellhead location [*Boyle and Zoback*, 2014, see Figure 3].

3 Seismicity Modeling

Time-dependent background seismicity rates are calculated for all $M_L \geq 1.5$ events using the temporal epidemic-type aftershock sequence (ETAS) model shown in equation 1:

$$\lambda(t, \theta) = \mu + \sum_{t_i < t} \frac{K e^{\alpha(M_i - M_c)}}{(t - t_i + c)^p} \quad (1)$$

where λ is the rate function, μ is the background seismicity rate, K is the aftershock productivity, α is the aftershock efficiency, c and p are the Omori decay parameters, and θ is a vector of (μ, K, α, c, p) [*Ogata*, 1992]. The ETAS model separates background events from the associated aftershocks and provides an estimate of the background earthquake occurrence rate for a given time interval. The best fit parameters for the rate function λ are computed by maximizing the log likelihood function shown in equation 2 [*Ogata*, 1992] for the event times and corresponding magnitude. We refer the reader to *Zhuang et al.* [2012] for a complete review of temporal ETAS models.

$$\ln L = \sum_{i=1}^{N} \ln \lambda(t_i) - \int \lambda(t) \, dt \quad (2)$$

Fitting the model variables is a nonlinear optimization problem, and we minimize the negative log likelihood using a quasi-Newton algorithm (fmin_bfgs function in the SciPy package). Upon convergence we estimate the covariance and standard deviation for each best fit parameter in the vector θ using equation 3 [*Ogata*, 1999].

$$\sigma^2 = (J^{-1}); \quad J_{ij} = \frac{\partial^2 \ln L}{\partial \theta_i \partial \theta_j} \quad (3)$$

Formally, ETAS model fitting requires solving for five free variables and can result in trade-offs between values giving unreasonable solutions that do not agree with Omori law, Gutenberg-Richter scaling, or the network used to develop the catalog. For the model fitting in this study we elect to hold α and c constant using a priori information due to the unstable nature of ETAS inversions for catalogs with significant swarm-like earthquake activity [*Brodsky and Lajoie*, 2013; *Hainzl and Ogata*, 2005]. The α value represents the aftershock productivity for a main shock, where values less than 1.0 indicate low aftershock productivity [*Felzer et al.*, 2004; *Helmstetter*, 2005]. Here we hold the α value constant at 0.75 based on previous studies analyzing seismicity in geothermal fields [*Hainzl and Ogata*, 2005; *Trugman et al.*, 2016]. We also perform all model calculations for an α value of 1.0 to ensure that we are not biasing the results by our parameter selection. The second value we hold constant is the c parameter, which depends on the seismic network detection threshold and for a given magnitude of completeness. To determine the c value we modify the approach described by *Brodsky and Lajoie* [2013]. See Figure S2 for a full description of the method. We hold the c parameter constant at 43 s, indicating that all events $M \geq 1.5$ beyond this time interval are observed following a main shock.

We estimate time-dependent earthquake background rates [*Brodsky and Lajoie*, 2013; *Hainzl and Ogata*, 2005; *Marsan et al.*, 2013; *Trugman et al.*, 2016] by fitting the ETAS model using a 6 month window of events and step through the time series in 1.0 month intervals. This procedure is performed for 1.0 km depth intervals from 1.0 km to 5.0 km with respect to mean sea level. With the use of discrete intervals for the event selection we anticipate some correlation due to event interaction between intervals and depth uncertainty. For our time series generation we find similar results when shortening the moving window to 4 months but observe short-term spikes in the time series of background rate μ when reducing to 3 months or less (see Figure S3). Extending the moving window to longer time intervals provides smoother rate curves and does not change our results. Therefore, we maintain the 6 month window for the analysis.

4 Seismicity Rates and Depth Dependence

The time series of monthly background seismicity rates for events between 1 and 5 km depths for the NW and SE study areas are shown in Figure 2 at 1 km depth intervals with the corresponding total monthly water injection

mass. The time series are shown with one standard error on the order of 0.1 events per day. The ETAS model results indicate that 89% of the earthquakes are independent events for both the NW and SE regions. The total number of events considered aftershocks changes by <0.5% when the α variable is held constant at 1.0 for the calculations. The rate curves indicate an annual period with peak seismicity rates following peak injection times. In the NW study area the rate curves indicate the highest seismicity rates and largest annual rate variations between 2 and 4 km, which is just below the injection well interval ranging from 0.9 to 1.5 km. The rate curves in the SE region are much lower with peak rates in the 1–3 km depth range, and annual fluctuations are resolvable down to about 4 km.
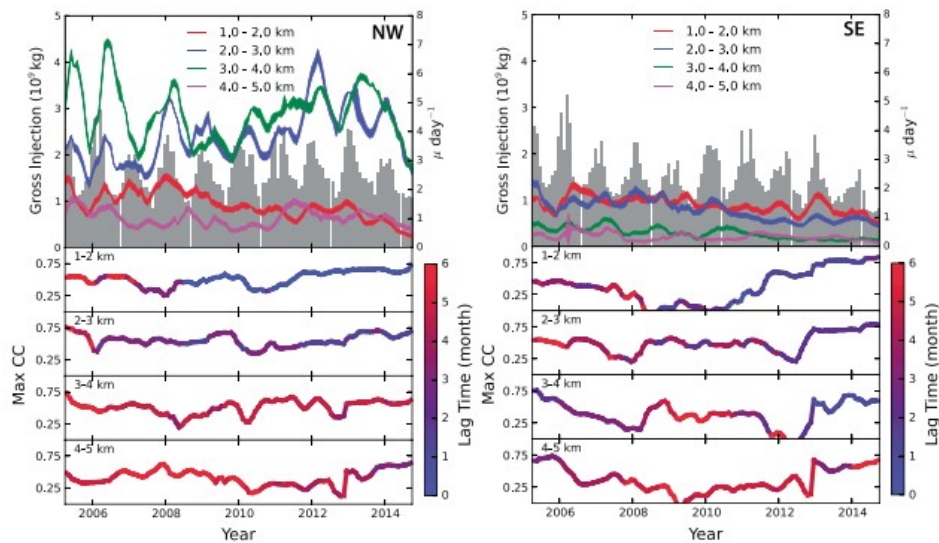
Figure 2. Background seismicity rates with monthly injection totals and cross-correlation time series shown as a function of depth for the (left) NW and (right) SE regions as indicated in Figure 1. The top frame shows the monthly seismicity rates with the depth interval indicated by color. The gray bars in the background are the gross monthly injection totals for the two regions. The seismicity rate curves are calculated using the ETAS model with a 6 month moving window stepping forward in 1 month increments. The half-width of the curve indicates one standard deviation from the estimated rate. The bottom plot shows the temporal variations in cross-correlation coefficients for the background seismicity rate and injection at each depth interval using a 48 month moving window. The color of the curve represents the time lag in months for the maximum correlation coefficient.

We perform a 48 month moving window cross-correlation analysis to compare the seismicity rates with the monthly totals of gross injection, gross production, and net injection (injection less production). Figure 2 shows the correlation coefficient and time lag for maximum correlation for the gross monthly injection. For the NW region, we find an increase in the mean time lag from 0 to 6 months with increasing depth. The time lag at greater depths agrees with *Beall et al.* [2010] observation of the occurrence of $M \geq 3$ events in the HTZ 3–5 months after peak injection. In the NW region of TG we find a correlation coefficient >0.5 for the 1–2 and 2–3 km depths for the study period with the exception of a few months in 2007 and 2010. For the 3–5 km depth intervals we also find good agreement but more variability shown by periods of low correlation. After 2007 the correlation values indicate a more systematic increase of time lag with increasing depth. The rate curves indicate fewer events per day in the 3–4 km depth range and that rate

decreases until 2010. The correlation curves for the SE region contain values above 0.5 for the 2–3 km depth range with a time lag between 2 and 5 months. Lower correlation with the injection is seen in the 1–2, 3–4, and 4–5 km depth intervals before 2013. Even with the variability and low correlation values we do observe a general trend of time lag increasing with depth. We test shorter-correlation windows and find similar results using a 24 month moving window and elect to show the smoother 48 month window (see Figure S4).

Additionally, we test for correlation with the production and the net totals (injection minus production) using the same procedure as described for the injection (see Figures S5 and S6). Our results indicate no correlation in the NW or SE region with the production values. The net injection totals produce nearly identical values as the injection since the steam production totals remain near constant throughout the year. We consider the injection as the main driver of the induced seismicity and do not explore further the production or net injection results.

The 10 years of $M \geq 1.5$ seismicity data are compiled by time of year and depth to illuminate the depth migration of seismicity with time using the entire catalog of events. Figure 3 shows the monthly average injection and production totals, the cumulative number of $M \geq 1.5$ events from the original catalog for every 0.5 km depth interval by 0.5 months, and the percent excess number of events in each bin for the NW and SE regions. The percent excess value is calculated by first reducing each depth interval by the depth interval average, then normalizing by the average number of events in that depth interval. Assuming downward fluid flow from the injection interval [*Gritto et al.*, 2014], we include three linear diffusion curves in Figure 3 using equation 4 for hydraulic diffusivity values (D) of 10.00, 1.00, and 0.10 $\mathrm{m^2\,s^{-1}}$ to indicate a possible range of effective hydraulic properties in the reservoir and estimate the diffusion distance (d).

$$d = \sqrt{Dt} \quad (4)$$
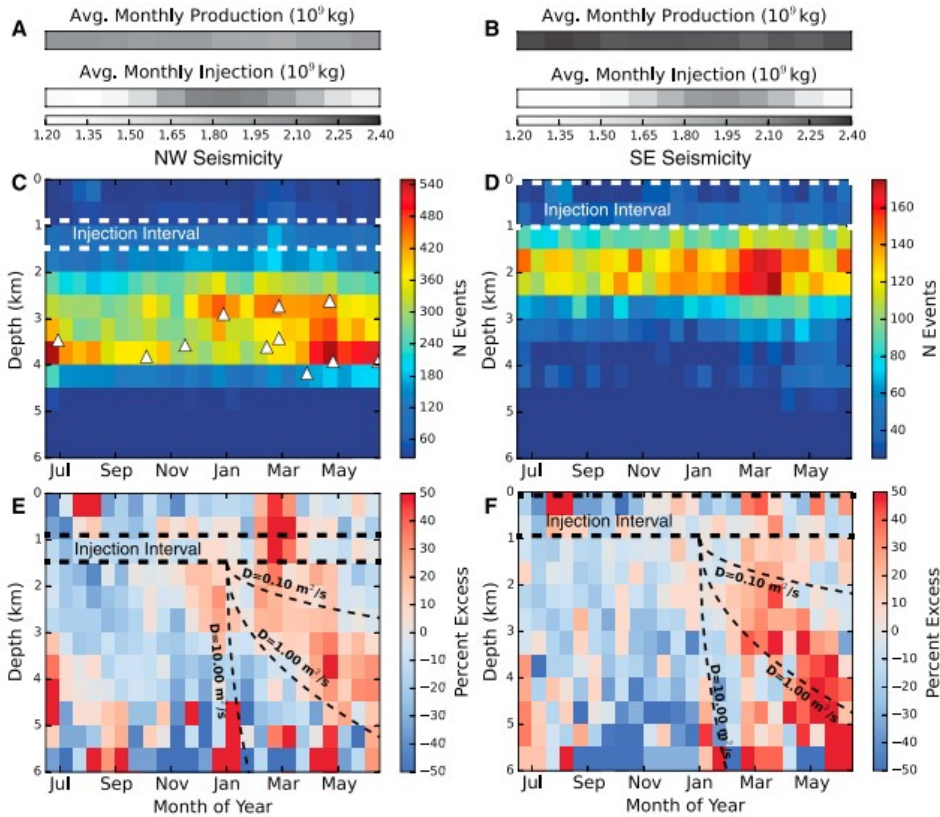
Figure 3. (a and b) The average monthly injection and production totals are shown for the NW and SE study areas in gray. Note that the *x* axes for Figures 3a and 3b align with the bottom plots and all are centered at December/January to more clearly represent the annual cycle of peak seismicity rates and fluid injection. The injection and production averages indicate peak injection in the winter months and production near constant throughout the year. The $M \geq 1.5$ events are shown by depth and time of year for the (c) NW and (d) SE study areas using a bin width of 0.5 months and 0.5 km using all cataloged events from January 2005 to December 2014. In the NW (Figure 3c), the time of year and depth of the $M_L \geq 4.0$ are shown as white triangles. (e and f) The percent above or below the average number of events for each depth interval is shown, where warm colors indicate more events and cool colors indicate fewer events. The injection interval depth is shown with a thick dashed line to indicate the depth of large-volume injection. The thin dashed black lines are for diffusivities of 0.10, 1.00, and 10.00 m²/s and correspond to the diffusion distance.

The diffusion curves are positioned at January, the peak month of injection, and a depth of 1.5 km for the NW and 0.9 km for the SE corresponding to the lower extent of the depth interval, where >90% of the injection wells are located [*Gritto et al.*, 2014].

The NW region indicates near-constant production throughout the averaged years and a peak in total injection in January (Figure 3a). The stacked seismicity in Figure 3c shows an increase of events in early November when monthly injection totals are increasing. Included are the time of year and depth of the $M_L \geq 4.0$ events in the NW region. The timing of the largest events corresponds to the maximum injection and increase in depth over time. The maximum number of events stays within the 2.0–3.5 km depth range for a period of ~2.5 months before migrating ~1 km deeper when injection totals begin to decline. Between February and June the greatest numbers of earthquakes are located at a depth of 3–4 km, which is much deeper than the injection depth interval of 1.5 km in the NW. The change in seismicity is an indication of fluid migration deeper into the reservoir. The deepening is more pronounced in Figure 3e with the normalized totals. We

focus on the months and depths with more than 40 events, and the excess events lie between the 0.1 and 1.0 m²s⁻¹ diffusion curves.

We observe similar patterns in the SE region with near-constant production and peak injection in January (Figure 3b). The number of events by depth (Figure 3d) is constrained to a shallower portion of the geothermal field, which agrees with the seismicity rate curves shown in Figure 2. Microseismic activity increases in November and peak activity occurs at ~2 km depth when injection totals are maximum during December and January. After ~4 months of high-volume injection, increases in seismicity are observed to depths of ~3.5 km. The normalized seismicity totals shown in Figure 3f indicate an excess number of events during the first 6 months of the year reaching a depth of >4 km. Similar to the NW, the peak excess event values concentrate between the 0.1 and 1.0 m²s⁻¹ diffusion curves. Below 4 km we find excess events above the 1.0 m²s⁻¹ diffusion curve, but this depth range contains less than 40 events per bin during the study.

5 Discussion and Conclusions

The use of the temporal ETAS model to characterize depth-dependent seismicity rates at TG allows for exploration of the spatiotemporal evolution and extent of induced seismicity in the reservoir. The seismicity rate curves show good correlation with fluid injection but are not observed to respond to the extraction of steam in either the NW or SE region of the geothermal field. This field-wide observation is consistent with wells in the northernmost region of TG [*Kwiatek et al.*, 2015, see Figure 9] and supports the notion that fluid injection is the main driver of induced seismicity at TG [*Majer et al.*, 2007, and references within].

In the NW region, the seismicity rates during 2005–2007 indicate a 2–5 month time lag for all depth intervals, while after 2007 there is no resolvable time lag in the shallow depth intervals (1–2 km), where most of the injection is occurring (Figure 2). Interestingly, *Gritto and Jarpe* [2014] find an ~1 year time lag in time-dependent V_P/V_S tomography results from the start-up of the Santa Rosa water injection project in 2004 until 2007, indicating a delayed elastic response to fluid injection. After 2007, the V_P/V_S results indicate no more time lag with injection. Our seismicity rates show that the time lags in the NW increase more uniformly with depth after 2007, indicating that more earthquakes are occurring near the injectors in both space and time as the reservoir becomes more saturated. *Beall et al.* [2010] suggest that the delay in elastic response is the time needed to fully saturate portions of the reservoir previously not receiving injection water. In the SE region, the correlation values increase and the time lags decrease in the shallow portions of the reservoir, after 2010 (Figure 2). The excess events shown in Figure 3f for the SE region suggest that fluid migration and triggering also extend to depths of ~5 km even though seismicity rates there are very low. The SE correlation curves exhibit more variability and probably reflect the true heterogeneity of injection activity not captured by our reservoir

partitioning. The main difference between the two regions is that more earthquakes are occurring in the NW compared to the SE, and as *Beall and Wright* [2010] point out, the occurrence of larger events is concentrated in the NW. We find that the $M_L \geq 4.0$ events follow the same general trend of deepening over time after peak injection (Figure 3c), and this suggests that a more connective fracture network exists in the NW region that extends into the HTZ in order to rupture a $M_L \geq 4.0$ earthquake.

The pattern of the onset and deepening of earthquakes in the field-wide study presented here is consistent with the evolution of seismic activity at individual wells documented in several recent studies. In the NW study area, previously offline, isolated injection wells were targeted in focused studies to monitor microseismic activity in response to injection. *Kwiatek et al.* [2015] find systematic deepening of seismicity at one well (P9), while seismicity at a second injection well (P29) did not exhibit deepening with time. Thermomechanical-hydromechanical models describing microseismicity patterns during an enhanced geothermal system (EGS) demonstration experiment for injection well (P32) in the NW region of TG suggest near-field cooling during flash boiling of water to steam, thereby contracting the host rock and producing strains large enough to trigger microseismicity [*Jeanne et al.*, 2014; *Rutqvist et al.*, 2013]. Additionally, *Jeanne et al.* [2014] observe the reactivation of subvertical fractures near the injection well that allow the propagation of fluids and infer that changes in poroelastic stress are responsible for elevated seismic activity farther from the injection location. *Jeanne et al.* [2015] estimate a diffusivity of $0.18\,\mathrm{m^2\,s^{-1}}$ for the EGS experiment at P32, whereas diffusivity estimates as high as $10.0\,\mathrm{m^2\,s^{-1}}$ have been reported for injection well P9 [*Martínez-Garzón et al.*, 2014]. We place diffusivity curves on the seasonal excess seismicity (Figure 3) and see a pattern consistent with depth migration of seismicity with diffusivities in the range of $0.1–1.0\,\mathrm{m^2\,s^{-1}}$ in both the NW and SE regions. The higher diffusivity value at P9 could be the result of multiple reactivated faults that are interconnected, thereby creating new hydraulic conduits as new areas of production are coming online in the unexploited parts of the NW region.

The vertical movement of fluids requires a network of preexisting pathways that are always present or reactivated during large-volume injection [*Barton et al.*, 1995]. The low porosity of the reservoir matrix (~2%) suggests that hydraulic conductivity is controlled by the large number of variable-sized fractures that are reactivated during injection [*Martínez-Garzón et al.*, 2014]. Outcrop samples from TG reveal randomly oriented fractures with mineralization implying relatively low permeability throughout the reservoir [*Sammis et al.*, 1992]. However, rock coring samples indicate a weak, highly fractured rock matrix suggesting an easily sheared material that could maintain hydraulically conductive conduits [*Lockner et al.*, 1982]. After decades of injection, the regional maximum horizontal compressive stress orientation still dominates the reservoir, consistent with a normal/strike-slip faulting regime in and surrounding TG [*Boyle and Zoback*, 2014]. This implies

that regional tectonic stresses have produced fracture networks that are in a favorable orientation to reactivate and provide steeply dipping fault planes for fluid transport.

The extent of the depth migration we observe can be described by the conceptual model put forth by *Stark* [2003] and supported by *Beall et al.* [2010], which suggests that earthquakes extending from injection depths to ~5 km in the HTZ are due to injected water that is not boiled due to the rapid cooling of the surrounding rocks. Excess water is then driven by gravitational flow to greater depths producing the time lag we observe in the seismicity rate curves. We observe the deepening of events in both the NW and SE. The deeper triggered events are a result of both thermoelastic and poroelastic stresses as the slow wave of fluid penetrates into the reservoir while decreasing the effective normal stress on preexisting faults. Our exploration of the spatiotemporal evolution of seismicity at TG supports the notion of a field-wide network of hydraulically conductive faults that provides steeply dipping fluid pathways to a few kilometers below the point of injection.

References

Aki, K. (1965), Maximum likelihood estimate of *b* in the formula log $N = a - bM$ and its confidence limits, *Bull. Earthquake Res.*, 43, 237– 239.

Barton, C. A., M. D. Zoback, and D. Moos (1995), Fluid flow along potentially active faults in crystalline rock, *Geology*, 23(8), 683– 686, doi:10.1130/0091-7613(1995)023<0683:ffapaf>2.3.co;2.

Beall, J. J., and M. C. Wright (2010), Southern extent of The Geysers high temperature reservoir based on seismic and geochemical evidence, *Geothermal Resour. Counc. Trans.*, 34, 1199– 1202.

Beall, J. J., M. C. Wright, A. S. Pingol, and P. Atkinson (2010), Effect of high rate injection on seismicity in The Geysers, *Geothermal Resour. Counc. Trans.*, 34, 1203– 1208.

Bender, B. (1983), Maximum likelihood estimation of *b* values for magnitude grouped data, *Bull. Seismol. Soc. Am.*, 73, 831– 851.

Boyle, K., and M. Zoback (2014), The stress state of the northwest Geysers, California geothermal field, and implications for fault-controlled fluid flow, *Bull. Seismol. Soc. Am.*, 104(5), 2303– 2312, doi:10.1785/0120130284.

Brodsky, E. E., and L. J. Lajoie (2013), Anthropogenic seismicity rates and operational parameters at the Salton Sea geothermal field, *Science*, 341(6145), 543– 546, doi:10.1126/science.1239213.

Convertito, V., N. Maercklin, N. Sharma, and A. Zollo (2012), From induced seismicity to direct time-dependent seismic hazard, *Bull. Seismol. Soc. Am.*, 102(6), 2563– 2573, doi:10.1785/0120120036.

Eberhart-Phillips, D., and D. H. Oppenheimer (1984), Induced seismicity in The Geysers geothermal area, California, *J. Geophys. Res.*, 89(B2), 1191– 1207, doi:10.1029/JB089iB02p01191.

Evans, D. M. (1966), The Denver area earthquakes and The Rocky Mountain Arsenal disposal well, *Mt. Geol.*, 3(1), 23– 36.

Felzer, K. R., R. E. Abercrombie, and G. Ekström (2004), A common origin for aftershocks, foreshocks, and multiplets, *Bull. Seismol. Soc. Am.*, 94(1), 88– 98, doi:10.1785/0120030069.

Gritto, R., and S. P. Jarpe (2014), Temporal variations of V_p/V_s ratio at The Geysers geothermal field, USA, *Geothermics*, 52, 112– 119, doi:10.1016/j.geothermics.2014.01.012.

Gritto, R., D. Dreger, O. Heidbach, and L. Hutchings (2014), Towards the understanding of induced seismicity in enhanced geothermal systems, 210, doi:10.2172/1154937.

Hainzl, S., and Y. Ogata (2005), Detecting fluid signals in seismicity data through statistical earthquake modeling, *J. Geophys. Res.*, 110, B05S07, doi:10.1029/2004JB003247.

Hartline, C. S., M. A. Walters, and M. C. Wright (2015), Three-dimensional structural model building, induced seismicity analysis, drilling analysis, and reservoir management at The Geysers geothermal field, Northern California, *Geothermal Resour. Counc. Trans.*, 39, 603– 614.

Healy, J., W. Rubey, D. Griggs, and C. Raleigh (1968), The Denver earthquakes, *Science*, 161(3848), 1301– 1310.

Helmstetter, A. (2005), Importance of small earthquakes for stress transfers and earthquake triggering, *J. Geophys. Res.*, 110, B05S08, doi:10.1029/2004JB003286.

Hutchings, L., B. Bonner, S. Jarpe, and A. Singh (2015), Micro-earthquake analysis for reservoir properties at the Prati-32 injection test, The Geysers,

California, Proceedings of the Fourtieth Workshop on Geothermal Reservoir Engineering, Stanford Univ., Stanford, Calif., 26-28 Jan.

Jeanne, P., J. Rutqvist, C. Hartline, J. Garcia, P. F. Dobson, and M. Walters (2014), Reservoir structure and properties from geomechanical modeling and microseismicity analyses associated with an enhanced geothermal system at The Geysers, California, *Geothermics*, 51, 460– 469, doi:10.1016/j.geothermics.2014.02.003.

Jeanne, P., J. Rutqvist, A. P. Rinaldi, P. F. Dobson, M. Walters, C. Hartline, and J. Garcia (2015), Seismic and aseismic deformations and impact on reservoir permeability: The case of EGS stimulation at The Geysers, California, USA, *J. Geophys. Res. Solid Earth*, 120, 7863– 7882, doi:10.1002/2015JB012142.

Kwiatek, G., P. Martínez-Garzón, G. Dresen, M. Bohnhoff, H. Sone, and C. Hartline (2015), Effects of long-term fluid injection on induced seismicity parameters and maximum magnitude in northwestern part of The Geysers geothermal field, *J. Geophys. Res. Solid Earth*, 120, 7085– 7101, doi:10.1002/2015JB012362.

Lockner, D. A., R. Summers, D. Moore, and J. D. Byerlee (1982), Laboratory measurements of reservoir rock from The Geysers geothermal field, California, *Int. J. Rock Mech. Min. Sci. Geomech. Abstr.*, 19(2), 65– 80, doi:10.1016/0148-9062(82)91632-1.

Majer, E. L., R. Baria, M. Stark, S. Oates, J. Bommer, B. Smith, and H. Asanuma (2007), Induced seismicity associated with enhanced geothermal systems, *Geothermics*, 36(3), 185– 222, doi:10.1016/j.geothermics.2007.03.003.

Marks, S. M., R. S. Ludwin, K. B. Louie, and C. G. Bufe (1978), Seismic monitoring at The Geysers geothermal field, California, *U.S. Geol. Surv. Open File Rep.* 78–798, 1–26.

Marsan, D., E. Prono, and A. Helmstetter (2013), Monitoring aseismic forcing in fault zones using earthquake time series, *Bull. Seismol. Soc. Am.*, 103(1), 169– 179, doi:10.1785/0120110304.

Martínez-Garzón, P., G. Kwiatek, H. Sone, M. Bohnhoff, G. Dresen, and C. Hartline (2014), Spatiotemporal changes, faulting regimes, and source parameters of induced seismicity: A case study from The Geysers geothermal field, *J. Geophys. Res. Solid Earth*, 119, 8378– 8396, doi:10.1002/2014JB011385.

Ogata, Y. (1992), Detection of precursory relative quiescence before great earthquakes through a statistical model, *J. Geophys. Res.*, 97(B13), 19,845– 19,871, doi:10.1029/92JB00708.

Ogata, Y. (1999), Seismicity analysis through point-process modeling: A review, *Pure Appl. Geophys.*, 155, 471– 507.

Rutqvist, J., P. F. Dobson, J. Garcia, C. Hartline, P. Jeanne, C. M. Oldenburg, D. W. Vasco, and M. Walters (2013), The Northwest Geysers EGS demonstration project, California: Pre-stimulation modeling and interpretation of the stimulation, *Math. Geosci.*, 47(1), 3– 29, doi:10.1007/s11004-013-9493-y.

Sammis, C. G., L. An, and I. Ershaghi (1992), Determining the 3-D fracture structure in The Geysers geothermal reservoir, Proceedings of the Seventeenth Workshop on Geothermal Reservoir Engineering, Stanford Univ., Stanford, Calif., 29-31 Jan.

Shi, Y., and B. A. Bolt (1982), The standard error of the magnitude-frequency *b* value, *Bull. Seismol. Soc. Am.*, 72(5), 1677– 1687.

Stark, M. (2003), Seismic evidence for a long-lived enhanced geothermal system (EGS) in The Northern Geysers reservoir, *Geothermal Resour. Counc. Trans.*, 27, 727– 731.

Stark, M. A. (1991), Microearthquakes: A tool to track injected water in The Geysers reservoir, Geothermal Resources Council Monograph on The Geyser Geothermal Field, *Spec. Rep. (17)*, 111–117.

Thurber, C. H. (1983), Earthquake location and three-dimensional crustal structure in the Coyote Lake area, central California, *J. Geophys. Res.*, 88(B10), 8226– 8236, doi:10.1029/JB088iB10p08226.

Trugman, D. T., P. M. Shearer, A. A. Borsa, and Y. Fialko (2016), A comparison of long-term changes in seismicity at The Geysers, Salton Sea, and Coso geothermal fields, *J. Geophys. Res. Solid Earth*, 121, 225– 247, doi:10.1002/2015JB012510.

Walters, M. A., and J. Combs (1992), Heat flow in The Geysers-Clear Lake geothermal area of Northern California, USA, Monograph on The Geysers Geothermal Field, 43–53.

Wiemer, S., and M. Wyss (2000), Minimum magnitude of completeness in earthquake catalogs: Examples from Alaska, the western United States, and Japan, *Bull. Seismol. Soc. Am.*, 90(4), 859– 869, doi:10.1785/0119990114.

Zhuang, J., D. Harte, M. J. Werner, S. Hainzl, and S. Zhou (2012), Basic models of seismicity: Temporal models, Community Online Resource for Statistical Seismicity Analysis, doi:10.5078/corssa-79905